Supplementary materials

The Cryosphere
Supporting Information for
Recent timescale transition from interannual to decadal variability in January sea ice area over the Bering Sea
Weibo Wang[1,2], Chunsheng Jing[1,2], and Junpeng Zhang[1,2]
[1] Ocean Dynamics Laboratory, Third Institute of Oceanography, Ministry of Natural Resources, Xiamen 361005, China; [2] Fujian Provincial Key Laboratory of Marine Physical and Geological Processes, Xiamen 361005, China
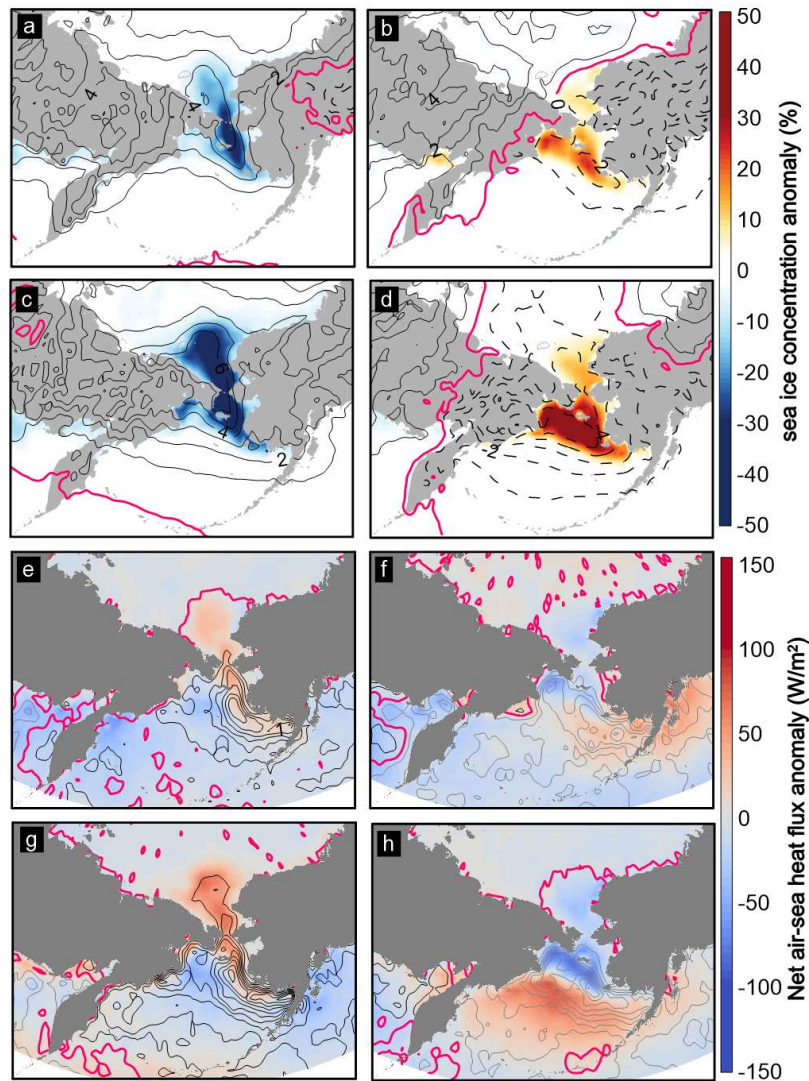
Figure S1. Same with Figure 6 in manuscript, but for surface air temperature, net air-sea heat flux, and sea surface temperature obtained from the ERA5 dataset.
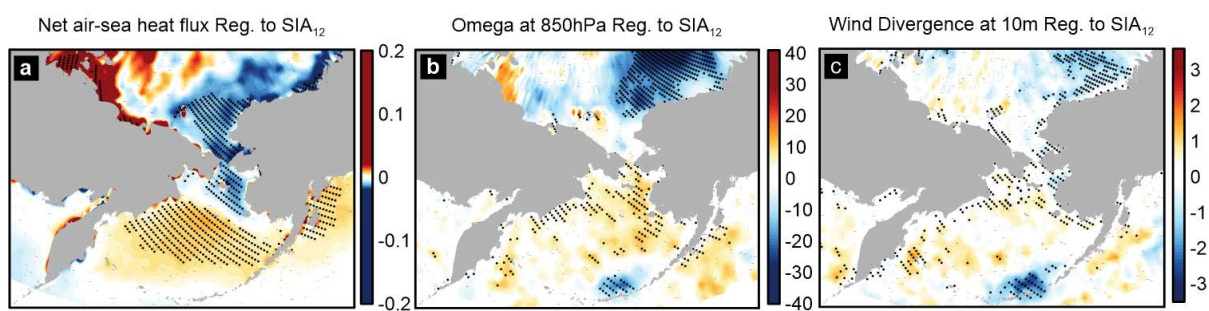
Figure S2. Same with Figure 7 in manuscript, but for sea level pressure, omega and wind vectors obtained from the ERA5 dataset.
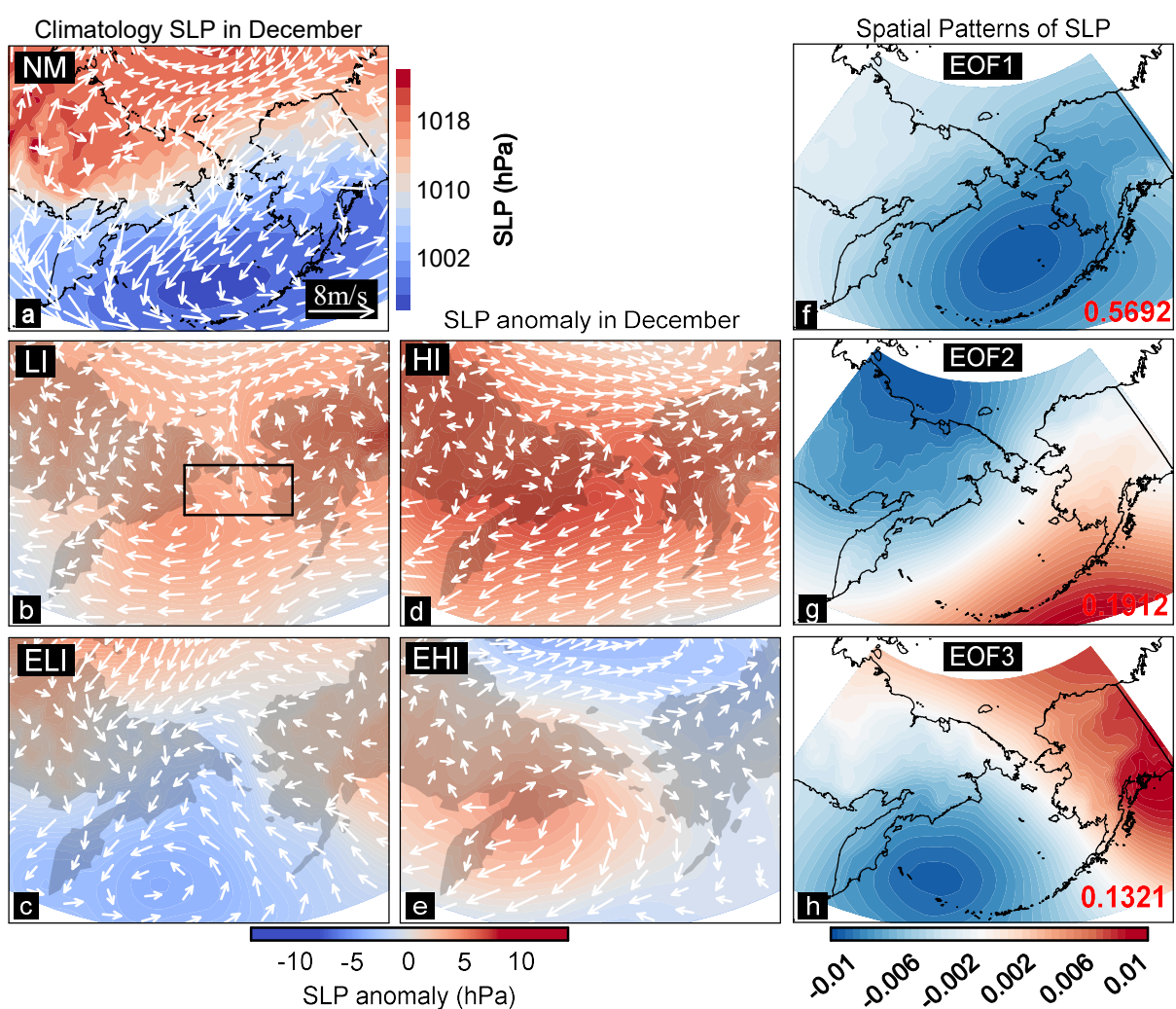
Figure S3. Same with Figure 8 in manuscript, but for sea level pressure and wind vectors obtained from the ERA5 dataset.
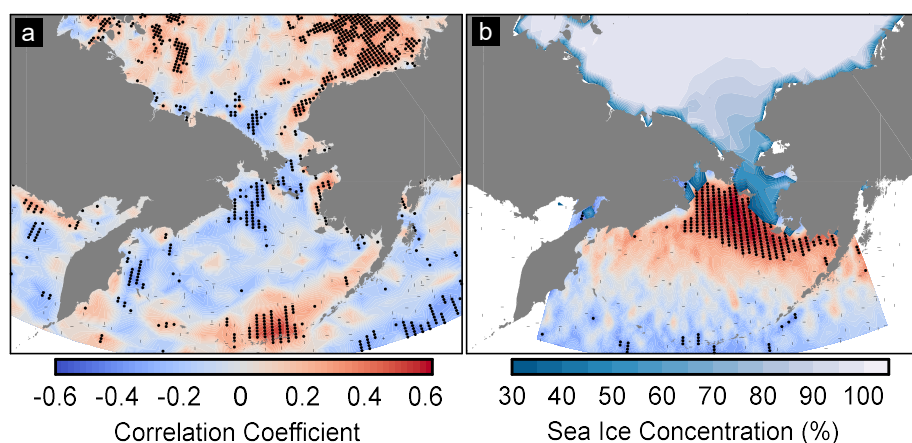
Figure S4. Same with Figure 9 in manuscript, but for the wind divergence and northward heat transport retrieved from the ERA5 dataset.
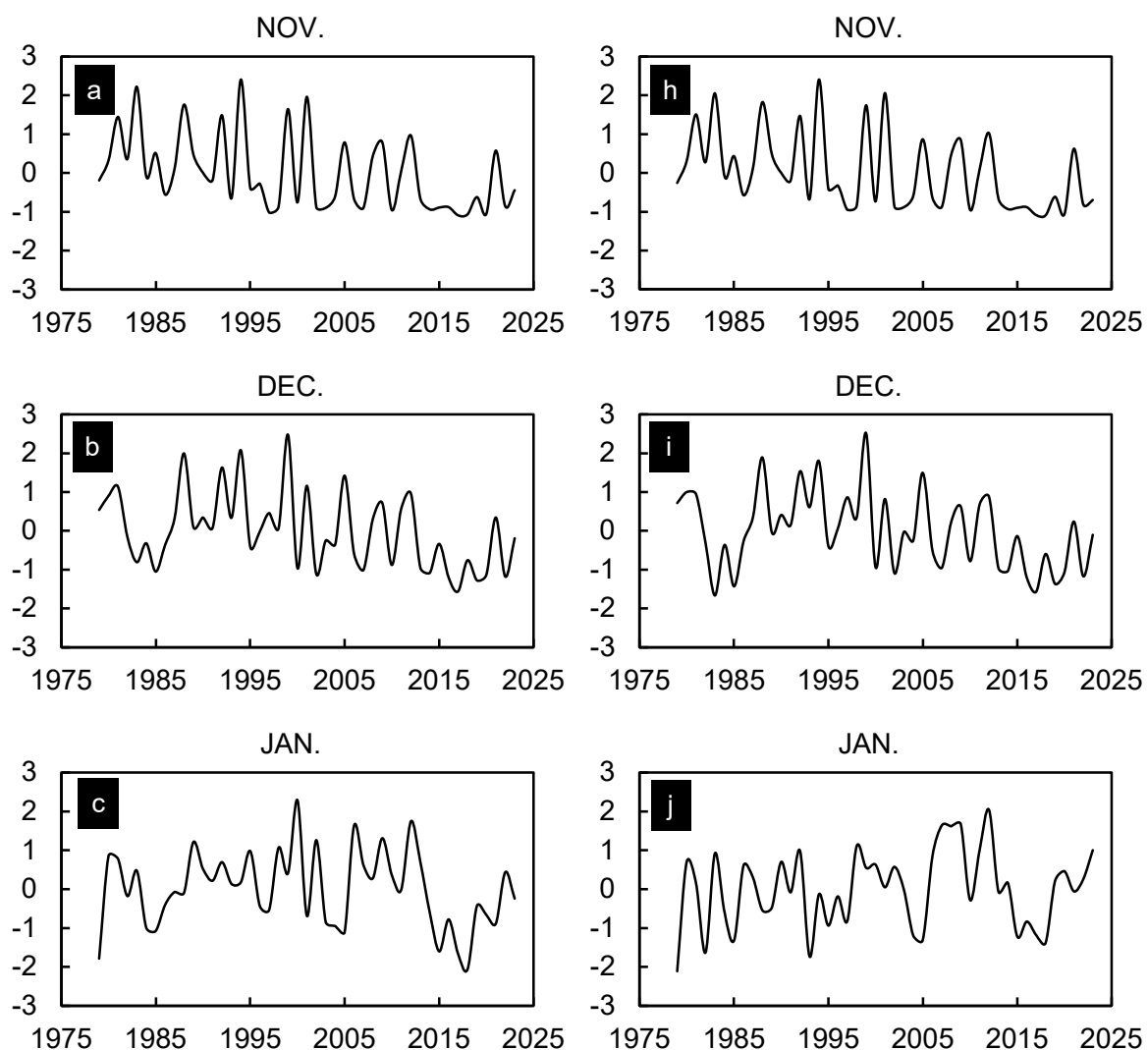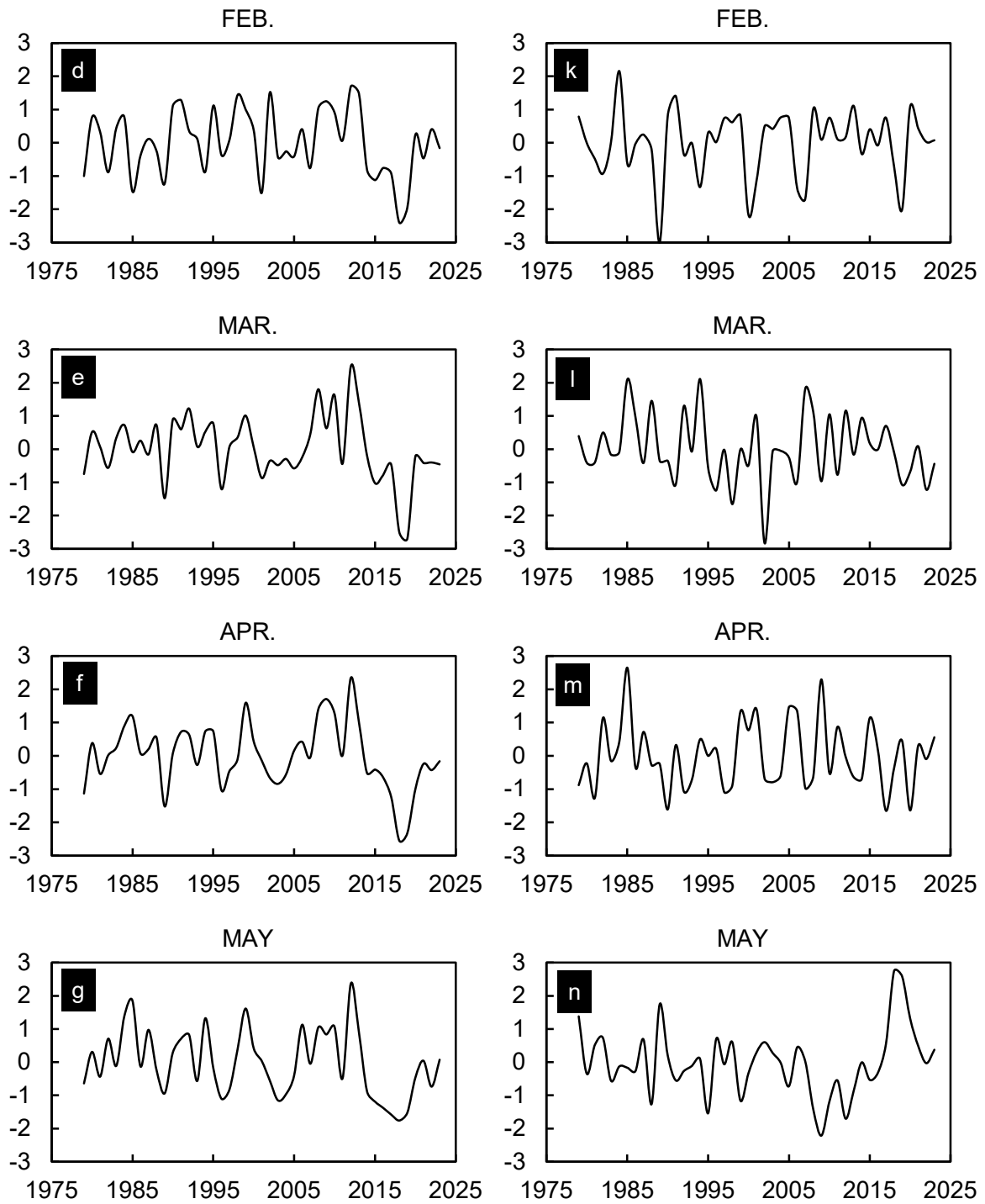
Figure S5. The time series of SIA (a~g) and △SIA (h~n) for each month from November to May.

S1. Multiscale variability of January ΔSIA anomalies derived from HADISST dataset

We selected the HADISST sea ice concentration dataset as supplementary validation to analyze the transition of January ΔSIA variability from interannual to decadal timescale in the Bering Sea.

The analysis covers the period 1953–2023, with spatial domains aligned to the study region. Utilizing the MODWT method, we decomposed the January ΔSIA anomalies into interannual, multiyear, and decadal components. Post-1979 data are specifically highlighted to align with the satellite observation era in Figure S6, ensuring cross-validation consistency with modern remote sensing records. Variance partitioning indicates that interannual-scale variability accounts for 38.6% of total fluctuations, while decadal-scale processes contribute 24.4%. A critical finding is the progressive intensification of decadal variability since 1990, suggesting a growing influence of decadal-scale climatic forcings on regional sea ice dynamics. These patterns exhibit strong concordance with results derived from the NSIDC sea ice concentration product.
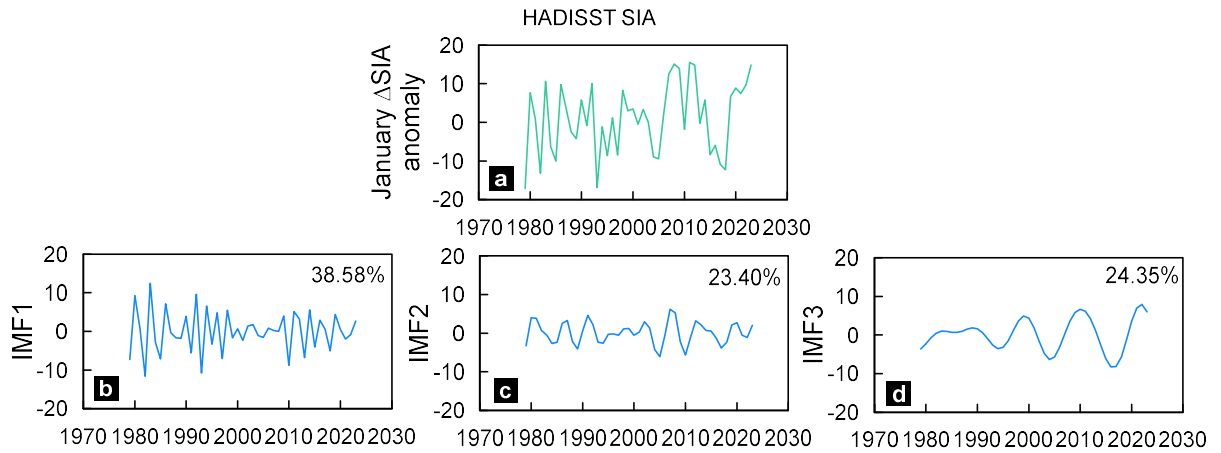
Figure S6. Multiscale variability of January HADISST ΔSIA anomalies characterized through: (a-c) Leading intrinsic mode functions (IMFs) showing variance contributions (numerical labels) to total ΔSIA variability;

S2. Morlet wavelet power spectrum analysis for the Bering Sea ΔSIA variability in January

Here, we employ the Morlet wavelet power spectrum analysis to investigate the timescale transition of ΔSIA in January. Our analysis provides the wavelet power spectrum, global wavelet spectrum, and scaled-average variation during the 8 to 15-year period, as shown in Figure S7. Through the examination of the wavelet power spectrum, it becomes evident that ΔSIA exhibits both interannual and decadal variations during the period from 1979 to 2021. Notably, the decadal variations predominantly occur after 1995. From 1979 to 2005, a gradual strengthening of the decadal signal in ΔSIA is observed, as indicated by the scaled-average time series. Subsequently, the decadal signal of ΔSIA persists above the 95% confidence level, signifying a sustained and robust long-term change.
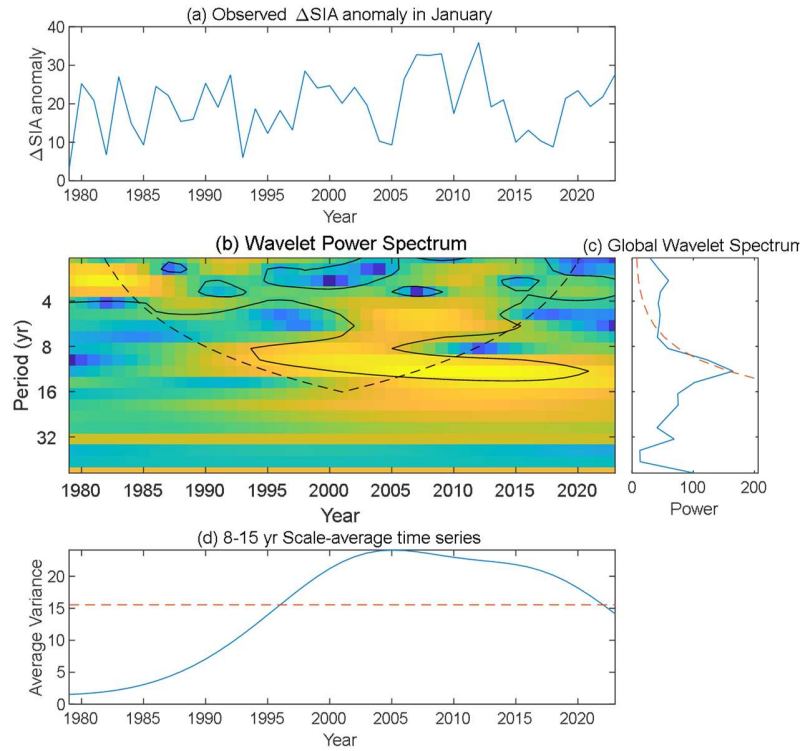
Figure S7. A comprehensive analysis of the Bering Sea ΔSIA variability in January using the Nasa-team sea ice concentration dataset. Panel (a) depicts the time series of ΔSIA in January; Panel (b) displays the morlet wavelet power spectrum of ΔSIA. Solid contours represent the 5% significance level, which is tested against red noise. The areas under cone-shaped lines are influenced by edge effect. Panel (c) shows global wavelet spectrum, with the dashed lines denoting the 5% significance level. Panel (d) highlights the average variance of ΔSIA in January during the 8 to 15-year period, with the red dashed line indicating the 5% significance level.

S3. The relationship between sea ice cover and air-sea net heat flux

In this analysis, we concentrate on the regions experiencing significant sea ice changes in December, as illustrated in Figure S8a. We have calculated the changes in air-sea heat flux within this region from 1979 to 2021, encompassing sensible heat flux, latent heat flux, net longwave radiation, net shortwave radiation, and net air-sea heat flux, as depicted in Figure S8b.
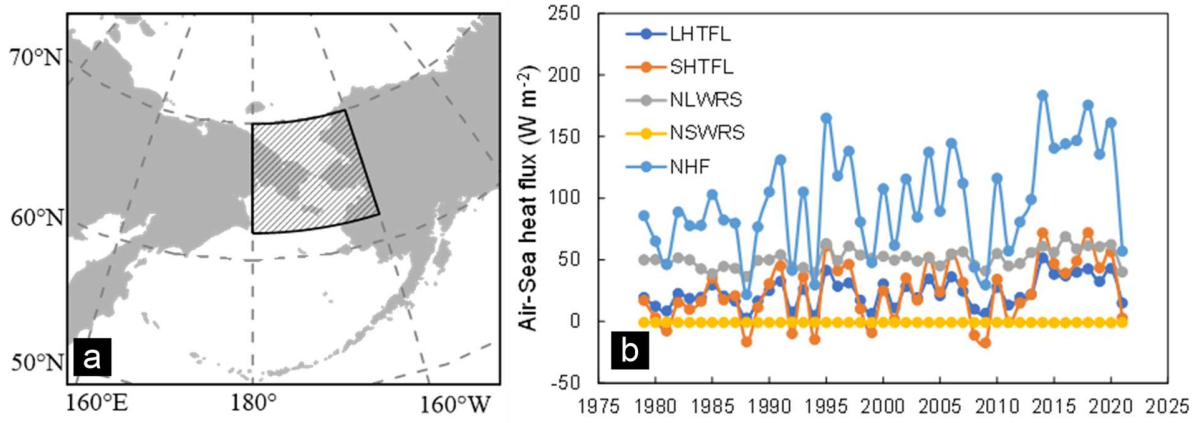
Figure S8. (A) Regions experiencing significant sea ice changes in December, highlighted by shaded areas. And (B) the mean sea-air heat flux within the region for the month of December, including sensible heat flux (represented by the orange line), latent heat flux (blue line), net longwave radiation (gray line), net shortwave radiation (yellow line), and the cumulative net sea-air heat flux (blue line).

Over the period 1979-2021, the average net shortwave radiation within the ROI was 0 W m^{-2}. The average net air-sea heat flux during this period reached 97.47 W m^{-2}. Among the contributing components, net longwave radiation exhibited the highest value, amounting to 50.83 W m^{-2}. A relatively minor difference was observed between sensible heat flux (23.85 W m^{-2}) and latent heat flux (23.57 W m^{-2}). On average, net longwave radiation accounted for 51.7% of the net air-sea heat flux. However, in terms of interannual variability, the change in net air-sea heat flux proved to be considerably more substantial than that of net longwave radiation. From 1979 to 2021, the variance of net air-sea heat flux was 1684.52 (W m^{-2})^2, while net longwave radiation exhibited a variance of merely 54.02 (W m^{-2})^2. These findings suggest that the interannual variability of net longwave radiation is insufficient to account for the observed changes in net air-sea heat flux.

To elucidate the substantial variance observed in the net air-sea heat flux, we employed the variance decomposition method proposed by Wang et al. (2022). This analytical approach allows for the identification of the individual contributions from each heat flux component to the overall variability in the net air-sea heat exchange. The mathematical formulation of this decomposition is provided below:

$$\sum(Q_{net} - \overline{Q_{net}})^2$$

$$= \sum\left((Q_{LHTFL} - \overline{Q_{LHTFL}}) + (Q_{SHTFL} - \overline{Q_{SHTFL}}) + (Q_{NSWRS} - \overline{Q_{NSWRS}})\right.$$

$$\left. + (Q_{NLWRS} - \overline{Q_{NLWRS}})\right)^2 \tag{1}$$

$$Var(Q_{net}) = Var(Q_{LHTFL}) + Var(Q_{SHTFL}) + Var(Q_{NSWRS}) + Var(Q_{NLWRS})$$
$$+ 2 \times Cov(Q_{SHTFL}, Q_{LHTFL}) + other \tag{2}$$

Here, 'Var' denotes variance, which is a measure of the spread or dispersion of a set of data points around their mean value. On the other hand, 'Cov' stands for covariance, a statistical term that quantifies the extent to which two variables are linearly related or change together.

Equation (2) elucidates that the variance of air-sea heat flux is composed of the variances of four distinct components, namely, sensible heat flux, latent heat flux, net longwave radiation, and net shortwave radiation. Additionally, the covariance between these four components also contributes to the overall variance. To quantify the relative importance of each term in Equation (2), we calculated the ratio of each term to the variance of the net air-sea heat flux. This ratio is defined as the variance contribution rate (VCR), which provides a measure of the proportionate impact of each component on the overall air-sea heat flux variability. The VCRs are graphically presented in Figure S9.
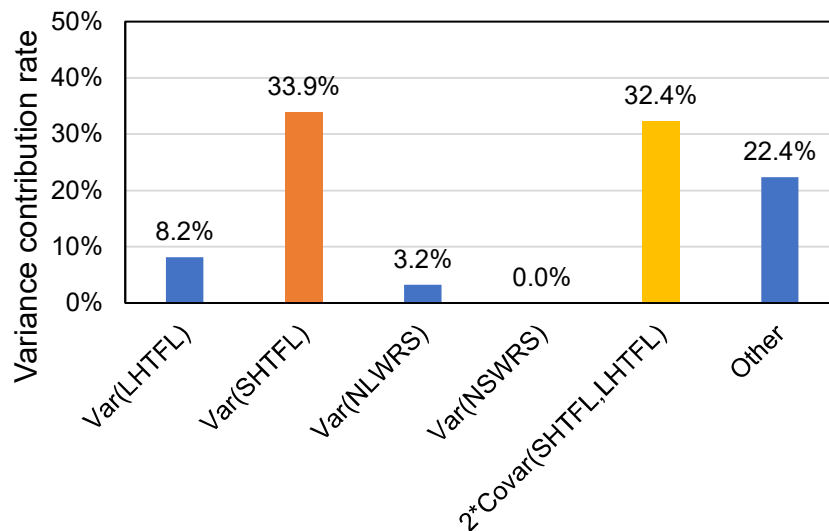
Figure S9. the variance contribution rates of sensible heat flux, latent heat flux, net longwave radiation, and net shortwave radiation to the net air-sea heat flux. The figure also depicts the variance contribution rates resulting from the covariance between sensible heat flux and latent heat flux, along with the cumulative variance contribution rates attributable to the remaining covariance terms.

Analysis of the VCRs reveals that the net longwave radiation exhibits a VCR of 3.2%, which is comparatively lower than the 8.2% VCR of latent heat flux. This finding corroborates that, despite the net longwave radiation having the largest magnitude among the air-sea heat flux components, it is not the primary driver of changes in the net air-sea heat flux within the ROI. The interannual variability of net air-sea heat flux is predominantly influenced by sensible heat flux, which displays a VCR of 33.9%. The synergistic interaction between sensible heat flux and latent heat flux is the second most significant contributor, with a VCR of 32.4%. Collectively, these results indicate that the interannual variability of air-sea heat flux within the ROI during December is primarily governed by the variability of sensible heat flux.

Subsequently, we examined the correspondence between the climate state sea ice concentration and sensible heat flux within the ROI. For this purpose, we partitioned sea ice concentration ranging from 0 to 100% into 11 distinct intervals and computed the average sensible heat flux corresponding to each bin in the region. The statistical results are presented in Figure S10. This graphical representation reveals that sensible heat flux does not exhibit a gradual decrease with increasing sea ice concentration. Instead, it displays a peak value within the sea ice concentration range of 20-30% and subsequently decreases towards negative values as sea ice concentration continues to increase. Notably, in the transition from ice-free conditions to a sea ice concentration of 30%, sensible heat flux experiences a gradual increase.
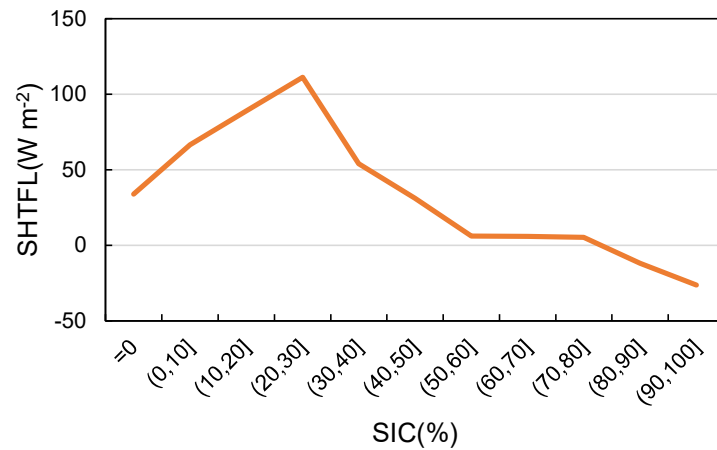
Figure S10. The mean sensible heat flux binned by sea ice concentration in the Pacific sector during December.

Based on the preceding analysis, we can construct a conceptual model to explain the observed net air-sea flux patterns in the ROI. Under extreme heavy ice conditions, the net air-sea flux within the ROI is minimal. As the sea ice coverage gradually declines, eventually reaching the levels observed in normal years, the marginal ice zone (MIZ) shifts northward. This transition is accompanied by a substantial increase in the net air-sea heat flux within the ROI. However, when sea ice extent decreases further to reach current extreme low-ice levels, the MIZ still remains within the ROI. As a result, the increase in net air-sea heat flux within the ROI is less pronounced compared to the transition from extreme heavy ice years to normal years. In future scenarios, as the MIZ extends beyond the boundaries of the ROI, it is likely that the net air-sea heat flux within the region will correspondingly decrease.